Time-resolved 2-million-year-old supernova activity discovered in Earth's microfossil record

Peter Ludwig[a], Shawn Bishop[a,1], Ramon Egli[b], Valentyna Chernenko[a], Boyana Deneva[a], Thomas Faestermann[a], Nicolai Famulok[a], Leticia Fimiani[a], José Manuel Gómez-Guzmán[a], Karin Hain[a], Gunther Korschinek[a], Marianne Hanzlik[c], Silke Merchel[d], and Georg Rugel[d]

[a]Physik Department, Technische Universität München, 85748 Garching, Germany; [b]Geomagnetism and Gravimetry, Central Institute for Meteorology and Geodynamics, 1190 Vienna, Austria; [c]Chemie Department, Fachgebiet Elektronenmikroskopie, Technische Universität München, 85748 Garching, Germany; and [d]Helmholtz-Zentrum Dresden-Rossendorf, Helmholtz Institute Freiberg for Resource Technology, 01328 Dresden, Germany

Edited by Edouard Bard, Centre Européen de Recherche et d'Enseignement des Géosciences de l'Environnement, Aix-en-Provence, France, and accepted by Editorial Board Member Anthony Leggett June 22, 2016 (received for review January 28, 2016)

Massive stars ($M \gtrsim 10\ M_{\odot}$), which terminate their evolution as core-collapse supernovae, are theoretically predicted to eject $>10^{-5} M_{\odot}$ of the radioisotope ^{60}Fe (half-life 2.61 Ma). If such an event occurs sufficiently close to our solar system, traces of the supernova debris could be deposited on Earth. Herein, we report a time-resolved ^{60}Fe signal residing, at least partially, in a biogenic reservoir. Using accelerator mass spectrometry, this signal was found through the direct detection of live ^{60}Fe atoms contained within secondary iron oxides, among which are magnetofossils, the fossilized chains of magnetite crystals produced by magnetotactic bacteria. The magnetofossils were chemically extracted from two Pacific Ocean sediment drill cores. Our results show that the ^{60}Fe signal onset occurs around 2.6 Ma to 2.8 Ma, near the lower Pleistocene boundary, terminates around 1.7 Ma, and peaks at about 2.2 Ma.

accelerator mass spectrometry | magnetofossils | supernova

The isotope ^{60}Fe is mostly produced during the evolution of massive stars ($M \gtrsim 10\ M_{\odot}$) in two steps along the course of their evolution. In the first step, during their quiescent helium and carbon shell burning phases, ^{60}Fe is synthesized at the base of these shells by a slow neutron capture process on preexisting stable seed nuclei, mostly by two successive neutron captures starting on stable ^{58}Fe (1). In the second step, shock heating within the carbon shell, driven by the passage of the supernova (SN) blast wave, allows for the synthesis of a modest amount of ^{60}Fe just before the subsequent disruption of the star and the concomitant explosive ejection of these shell mass zones, and the ^{60}Fe within them, into the interstellar medium. The subsequent beta-decay of ^{60}Fe, which has a half-life of $t_{1/2} = (2.61 \pm 0.04)$ Ma (weighted average of refs. 2 and 3), gives rise to two characteristic gamma-ray lines, which have been detected in the central part of the galactic plane (4), known to be a site of massive stars, confirming the association of ^{60}Fe formation with regions of ongoing massive star nucleosynthesis.

If a core-collapse SN (CCSN) occurs sufficiently close to our solar system, part of the ejected matter should arrive in our solar system. The best candidate mechanism for overcoming the solar wind pressure and penetrating to Earth's orbit is dust transport (5, 6). Recent investigations with far-infrared to submillimeter telescopes suggest that CCSN ejecta are efficient dust sources (7). For instance, copious amounts of dust with a large mass fraction contained in grains of above 0.1 μm size (and up to 4.2 μm) have recently been observed in the ejecta of SN 2010jl (8). During atmospheric entry, dust grains are expected to be partially or totally ablated, depending on composition, incident velocity, and angle of entry (9). The ^{60}Fe released in the ablated fraction will enter the terrestrial iron cycle (10) and become deposited into geological reservoirs such as marine sediments.

An excess of ^{60}Fe was already observed in ~2-Ma-old layers of a ferromanganese (FeMn) crust retrieved from the Pacific Ocean (5, 11, 12) and, recently, in lunar samples (13). However, due to the slow growth rate of the FeMn crust, the ^{60}Fe signal had a poor temporal resolution. This ^{60}Fe has been attributed to a deposition of SN ejecta; however, this interpretation has been challenged by an alternate hypothesis attributing the ^{60}Fe excess to micrometeorites (ref. 14, and references therein). An independent indication of a 2-Ma-old SN interaction with our solar system was recently deduced from the spectra of cosmic ray particles (15). In our work herein, we aimed at the analysis of the entire temporal structure of the ^{60}Fe signature in terrestrial samples. This requires a geological reservoir with an excellent stratigraphic resolution and high ^{60}Fe sequestration and low Fe mobility, which preserves ^{60}Fe fluxes as they were (or nearly so) at the time of deposition, apart from radioactive decay. Both conditions were fulfilled in the carefully selected marine sediments used in this study.

One particularly interesting mechanism by which Fe is sequestered within sediments is through biomineralization, e.g., by dissimilatory metal-reducing bacteria (DMRB) (16), and by magnetotactic bacteria (MTB) (17). MTB are single-cell prokaryotes, which produce intracellular chains of magnetite (Fe_3O_4) nanocrystals called magnetosomes (18, 19). These bacteria achieve their highest population densities near the so-called oxic–anoxic transition zone (20), where the oxygen concentration drops, producing a well-defined redox boundary. In pelagic sediments, this boundary occurs within a few centimeters below the sediment–water interface (21), forcing the MTB populations to move upward as the sediment column grows, with dead cells being left behind. After decomposition of the dead cells, the magnetosomes remain

Significance

Massive stars, which terminate their evolution in a cataclysmic explosion called a type-II supernova, are the nuclear engines of galactic nucleosynthesis. Among the elemental species known to be produced in these stars, the radioisotope ^{60}Fe stands out: This radioisotope has no natural, terrestrial production mechanisms; thus, a detection of ^{60}Fe atoms within terrestrial reservoirs is proof for the direct deposition of supernova material within our solar system. We report, in this work, the direct detection of live ^{60}Fe atoms in biologically produced nanocrystals of magnetite, which we selectively extracted from two Pacific Ocean sediment cores. We find that the arrival of supernova material on Earth coincides with the lower Pleistocene boundary (2.7 Ma) and that it terminates around 1.7 Ma.

Author contributions: S.B. designed research; P.L., S.B., R.E., B.D., T.F., N.F., L.F., J.M.G.-G., K.H., G.K., M.H., S.M., and G.R. performed research; P.L., V.C., M.H., S.M., and G.R. developed chemical techniques/protocols; P.L. and R.E. analyzed data; and P.L., S.B., and R.E. wrote the paper.

The authors declare no conflict of interest.

This article is a PNAS Direct Submission. E.B. is a Guest Editor invited by the Editorial Board.

[1]To whom correspondence should be addressed. Email: shawn.bishop@tum.de.

This article contains supporting information online at www.pnas.org/lookup/suppl/doi:10.1073/pnas.1601040113/-/DCSupplemental.

embedded within the sediment bulk and are subsequently called magnetofossils (22).

The ablated Fe fraction of SN dust grains arriving in the oceans is expected to undergo dissolution and reprecipitation upon reaching the sediment in the form of nanominerals, such as poorly crystalline ferric hydroxides (10). The poor solubility of Fe(III) minerals at circumneutral pH values (~0.1 nmol/L) means that Fe is hardly mobilizable under oxygenated conditions. Many microorganisms, including DMRB and MTB, get around this problem by excreting organic compounds known as siderophores, which specifically complex Fe(III). DMRB reduce Fe(III) to highly soluble Fe(II), which, in turn, leads to the precipitation of new minerals, among which is magnetite (Fe_3O_4) (16). Other bacteria perform Fe(II) oxidation (23). The Fe uptake capability of DMRB from particulate sources depends on the type of source mineral and particle size. Poorly crystalline hydroxides, such as ferrihydrite (FeOOH), are preferred over goethite (α-FeOOH) and hematite (α-Fe_2O_3), and Fe reduction rates are proportional to the specific surface area of particles (24–26). In particular, surface normalized bacterial Fe-reducing reaction rates are ~1.5 to 2 orders faster (26) for nano-sized ferrihydrite particles compared with grains with sizes comparable to bulk detrital grains. The Fe uptake capability of MTB has been investigated less extensively. Common constituents of the DMRB iron metabolism, such as genes for ferrous and ferric iron uptake, siderophore synthesis, and iron reductases, as well as iron-regulatory elements, are present in MTB (19). MTB are therefore able to take up ferric and ferrous iron from various sources (27) with similar capabilities as for DMRB. This is also supported by the fact that MTB are the main source of one reduction product—magnetite—in many types of sediments (28–31). The combination of Fe-reducing and Fe-oxidizing reactions supports the Fe cycle in sediments, yielding ultrafine (<100 nm) secondary Fe minerals (32, 33) (*Supporting Information*).

MTB extant at the time of SN ^{60}Fe input to the ocean floor are expected, therefore, to have incorporated ^{60}Fe into their magnetosomes, biogenically recording the SN signal (34). Unlike other Fe minerals and biomineralization products, magnetofossils have unique magnetic signatures enabling their detection down to mass concentrations in sediment of the order of few parts per million (29). As an essential point for this work, magnetofossil preservation ensures that the ^{60}Fe signal is not altered, because the very existence of these microfossils means that postdepositional Fe mobilization through reductive diagenesis (28, 35) did not occur.

In general, Fe(III) sources accessible to bacterial reduction can be extracted with buffered solutions of reducing agents such as citrate–bicarbonate–dithionite (CBD) and, to a lesser extent, ammonium oxalate (36). The CBD protocol (37) has been specially conceived to selectively dissolve fine-grained (<200 nm) secondary oxides in soils, but not larger particles of lithogenic origin (38, 39) (see *Supporting Information*). Therefore, CBD can be used to selectively extract Fe from magnetofossils and other secondary minerals along with ^{60}Fe, thereby minimizing any dilution from large-grained, ^{60}Fe-free primary mineral phases.

Materials and Methods

In our search for a biogenic SN signal, we selected two sediment cores, core 848 and core 851, from the equatorial Pacific (2°59.6′S, 110°29′W, 3.87 km water depth), recovered by the Ocean Drilling Program (ODP) during Leg 138 (40). The sediment of both cores is a pelagic carbonate (60% to 80% $CaCO_3$, 20% to 30% SiO_2) with a total iron content of 1.5 wt% to 3.5 wt% (41). Both cores are characterized by an excellent biostratigraphic and magnetostratigraphic record and almost constant sedimentation rates of (6.1 ± 0.1) m/Ma and (19.3 ± 0.2) m/Ma for cores 848 and 851, respectively, over the 1.7- to 2.7-Ma age range of interest (42), as shown in Fig. 1.

The presence of magnetofossils in these cores was confirmed by electron microscopy and magnetic analysis techniques based on first-order reversal curve (FORC) measurements (29, 34) (see *Supporting Information* and Figs. S1–S4). The average magnetofossil Fe concentration over the 1.7-Ma to 3.4-Ma interval was determined to be 25 μg/g to 30 μg/g for core 848, and 15 μg/g to 20 μg/g for core 851. Along with a constant sedimentation rate (Fig. 1) and sediment composition (43), the lack of significant magnetofossil concentration variations (see *Supporting Information* and Fig. S1), both absolute and relative to other magnetic Fe minerals, indicates that the depositional environment was stable during the period under investigation. An additional confirmation of stable sedimentation conditions was obtained by measurements of the ^{10}Be/^{9}Be ratio in representative samples of core 851, which show no significant deviation from exponential radioactive decay (see *Supporting Information*).

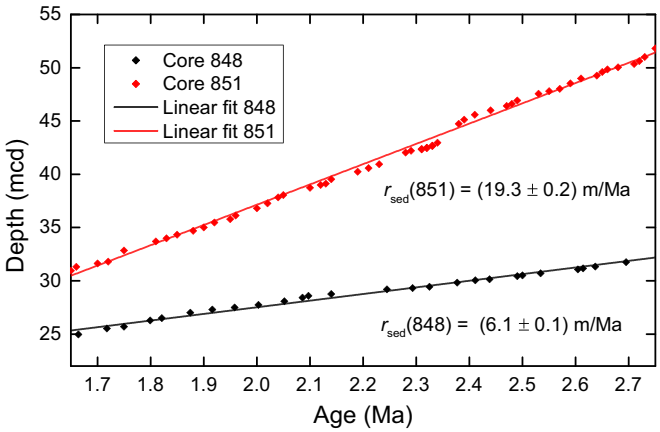

Fig. 1. Age model data of ODP drill cores 848 and 851 with linear fits overlaid. The *x* axis represents the depth in the respective drill cores in meters core depth (mcd). The slopes of the fits yield sedimentation rates as shown. No significant departure from linearity is observed across the displayed time range, indicating that both cores had constant sedimentation rates. The errors represent 1σ SDs. Data courtesy of ref. 42.

To maximize the ^{60}Fe/Fe atom ratio, a highly selective version of the CBD protocol (37) was developed (see *Supporting Information*); it is a very mild chemical leaching technique, able to completely dissolve secondary iron oxides such as magnetofossils, while leaving larger grains, which may not contain ^{60}Fe, essentially intact (29). At least 27% of the total Fe extracted with this technique is contained in magnetofossils (29), which therefore represent a significant contribution to the analyzed Fe pool. Even with this carefully designed extraction protocol, the expected ^{60}Fe concentrations are so low that the only viable measurement technique is ultrasensitive accelerator mass spectrometry (AMS), which has been carried out at the Gas-filled Analyzing Magnet System (GAMS) setup (44) at the Maier-Leibnitz-Laboratory (MLL) in Garching, Germany, over several beamtimes. The MLL features a 14-MV MP Tandem accelerator with an energy stability of $\Delta E/E \approx 10^{-4}$. For AMS measurements of ^{60}Fe, the samples are prepared as Fe_2O_3 powder mixed 50/50 by volume with Ag powder (120 mesh, lot J07W011; Alfa Aesar), which is subsequently hammered into a 1.5-mm-wide hole, drilled into a silver sample holder.

Fe was extracted as FeO^- from a single-cathode, cesium sputter ion source, and was injected into the accelerator after a preacceleration to 178 keV. The tandem terminal voltage for the experiments described here ranged between 11 MV and 12 MV, which favored selection of the charge state 10^+ for the radioisotope ^{60}Fe after passing through a 4-μm-thick carbon stripper foil at the accelerator terminal. A charge state of 9^+ was selected for the stable beam of ^{54}Fe, because it has nearly the same magnetic rigidity as $^{60}Fe^{10+}$ at nearly the same terminal voltage. After acceleration to 110 MeV to 130 MeV (depending on the available terminal voltage), the ions exit the accelerator and pass through a 90 degree dipole magnet for selection of the correct magnetic rigidity, and subsequently pass through two Wien velocity filters. Finally, the ions are directed toward the dedicated GAMS beamline by way of a switching magnet. Through use of the GAMS magnet, the challenging suppression of the stable isobar ^{60}Ni is achieved.

The GAMS magnet chamber is filled with 4 mbar to 7 mbar of N_2 gas. Through electron exchange reactions with the N_2 gas, each ion species adopts an equilibrium charge state distribution that depends on its atomic number *Z*. Thus, isobars will be forced on different trajectories if a magnetic field is applied. Because ^{60}Fe and ^{60}Ni have $\Delta Z = 2$, their trajectories on the exit side of the magnet can be spatially separated by 10 cm. The GAMS magnetic field can then be adjusted to make ^{60}Fe enter the particle identification detector, while most ^{60}Ni is blocked using a suitable aperture in front of the detector entrance. The detector itself is an ionization chamber featuring a Frisch grid and a fivefold split anode and is filled with 30 mbar to 50 mbar of isobutane as an

ionization medium. Individual ^{60}Fe ions can thus be identified by their energy deposition (Bragg curve), which is described in more detail in *Supporting Information*.

For measurements of the atom ratio ^{60}Fe/Fe, the stable beam of $^{54}Fe^{9+}$ is tuned into a Faraday cup in front of the GAMS, where the typical electrical current is 30 nA to 150 nA (sample-dependent). Then, the tandem terminal voltage and the injector magnet are switched to allow $^{60}Fe^{10+}$ to pass, and the Faraday cup is retracted. The ^{60}Fe ions are then individually identified and counted in the ionization chamber, while the ^{60}Ni background count rate is only about 10 Hz to 100 Hz. In this manner, a highly selective discrimination of ^{60}Fe against ^{60}Ni and other background sources is achieved, as demonstrated by the extremely low blank levels obtained with different blank materials, such as processing blanks and environmental samples. The concentration of ^{60}Fe/Fe is calculated from the number of ^{60}Fe events counted by the detector, the measurement time, and the average current of $^{54}Fe^{9+}$ in front of the GAMS. The transmission efficiency between the Faraday cup and the ionization chamber is canceled out by relating the measured concentration to the known concentration of a standard sample, which is measured periodically during a beamtime. For this work, the standard sample PSI-12, with a concentration $^{60}Fe/Fe = (1.25 \pm 0.06) \times 10^{-12}$, was used (see *Supporting Information*). The transmission efficiency of the entire system (including ion source yield, stripping yield, ion optical transmissions, and software cuts) during ^{60}Fe measurements is in the range $(1–4) \times 10^{-4}$.

Results

A total of 111 sediment samples (67 from core 848 and 44 from core 851), each with a mass of ~35 g, were treated with our CBD protocol, yielding ~5 mg AMS samples consisting of Fe_2O_3. Each AMS sample was measured for an average of 4 h until the sample material was exhausted, yielding one ^{60}Fe event, on average, and a total of 86 events integrated over both cores (42 in core 848 and 47 in core 851). Details of the ^{60}Fe event selection analysis can be found in *Supporting Information* and Figs. S5 and S6. Thus, several AMS samples have been grouped together to increase counting statistics, and our ^{60}Fe/Fe results are displayed in Fig. 2. Owing to the availability of several near-surface (0 Ma to 1 Ma) and very deep (7 Ma to 8 Ma) samples in core 848, the presence of a distinct ^{60}Fe signal could be clearly identified (Fig. 2*A*). The data are complemented by the observation of a similar signal in core 851 (Fig. 2*B*), which is characterized by a ~1.5 times lower ^{60}Fe/Fe ratio. The onset of the ^{60}Fe signal occurs at (2.7 ± 0.1) Ma and is centered at (2.2 ± 0.1) Ma. The signal termination is not as clear, because it remains slightly above the 1σ blank level until around 1.5 Ma, according to the data grouping used in Fig. 2*A*. A detailed analysis averaging over both sediment cores and several data groupings yields a more conservative estimate for the termination time of (1.7 ± 0.2) Ma; this results in a (1.0 ± 0.3) Ma long exposure of the Earth to the influx of ^{60}Fe. The ^{60}Fe flux, concomitant with the data of Fig. 2, is shown in Fig. S7 (see *Supporting Information* for its derivation).

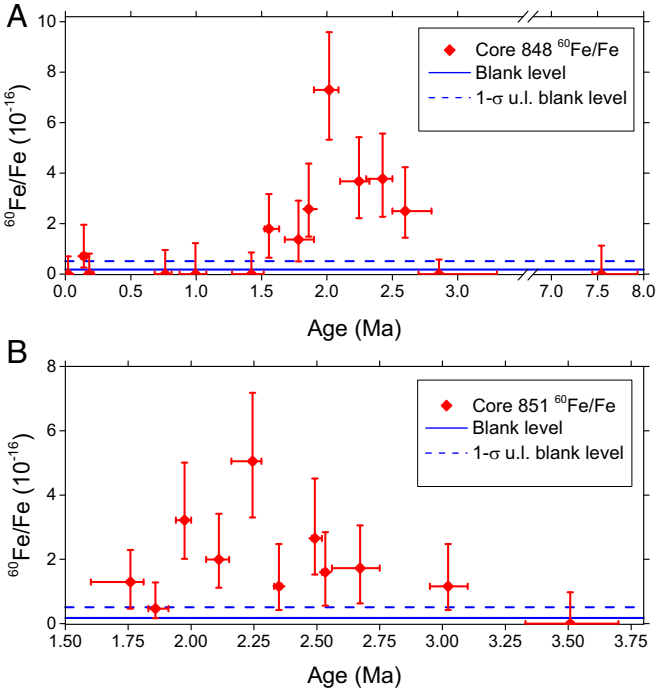

Fig. 2. The ^{60}Fe/Fe atom ratio determined in all sediment samples of cores (*A*) 848 and (*B*) 851. The *y* error bars indicate 1σ statistical uncertainties. The *x* axis ranges were chosen according to the availability of sample material. The *x* error bars represent core depth of sample material used for each data point. Each data point contains three to six adjacent individual AMS samples grouped together. The blank level and its 1σ upper limit (u.l.) are shown for a chemical processing blank. Note that *A* has a broken time axis relative to *B*.

An overview of the collected AMS data split into three age regions (<1.8 Ma, 1.8 Ma to 2.6 Ma, >2.6 Ma) is shown in Table 1. An estimate for the significance of the ^{60}Fe signal in the peak region can be obtained by applying the procedure suggested by ref. 45 for the superposition of two Poisson processes (i.e., signal and background). As a control region (no expected signal), we selected (*i*) the processing blank and, for comparison, (*ii*) the <1.8-Ma age interval of each respective sediment core. The second choice is rather conservative, because this overestimates the background signal. In the case of *i*, the procedure yields a significance (in multiples of σ) of 5.2 and 3.9 for cores 848 and 851, respectively. In the case of *ii*, these values become 7.2 and 2.0 (after subtraction of the blank level). The significance for core 851 is low in the case of *ii*, because only little data were collected in the control region.

A useful measure for the intensity of the total ^{60}Fe exposure is given by the terrestrial (Φ_{ter}) fluence of ^{60}Fe. Φ_{ter} represents the time-integrated, decay-corrected flux of ^{60}Fe into a given terrestrial reservoir over the entire exposure time. To sum up the contributions of all sediment layers in the signal range, the following integral is computed to calculate the average concentration of ^{60}Fe/Fe in the signal range:

$$\bar{C} = (t_2 - t_1)^{-1} \int_{t_1}^{t_2} C(^{60}\mathrm{Fe/Fe})\mathrm{d}t \qquad [1]$$

The average terrestrial ^{60}Fe fluence, Φ_{ter}, is then given by

$$\Phi_{ter} = \bar{C} \rho r_{sed} (t_2 - t_1) Y_{CBD} N_A / W_{Fe}, \qquad [2]$$

where ρ is the dry sediment density, r_{sed} is the sedimentation rate, Y_{CBD} is the efficiency-corrected CBD yield of extracted iron per unit mass of dry sediment, N_A is Avogadro's number, and W_{Fe} is the molecular weight of iron. Using $(t_2 - t_1) = (1.0 \pm 0.3)$ Ma as a nominal signal duration results in a terrestrial fluence into our sediments of $\Phi_{ter}^{848} = (4.7 \pm 1.6) \times 10^5$ atoms per square centimeter (at/cm^2) and $\Phi_{ter}^{851} = (8.8 \pm 2.9) \times 10^5$ at/cm^2 for cores 848 and 851, respectively. The slightly different values and larger errors compared with Table 1 result from an averaging over different exposure times $(t_2 - t_1)$, whereas the fluences in Table 1 were calculated for a fixed $(t_2 - t_1) = 0.8$ Ma. For the following discussion, we use the error-weighted mean of the fluences determined in both sediment cores, which is $\Phi_{ter}^{sed} = (5.6 \pm 1.8) \times 10^5$ at/cm^2 (taking into account an additional 10% uncertainty for the signal duration).

To compare this result with the fluence obtained by ref. 11 for the Pacific Ocean FeMn crust, several correction factors must first be applied. Since those results were published, the half-life of ^{60}Fe has undergone a revision (2, 3); the half-life of ^{10}Be, which was used to convert the crust growth rate to geological time, has also been redetermined (46, 47). A correction for the different ^{60}Fe standard samples used (which became available due to advanced cross-calibration measurements) must also be taken into account. The resulting, decay-corrected, terrestrial fluence derived from

Table 1. Summary of all ^{60}Fe data presented in this work

Sample	Age range, Ma	Number of samples	^{60}Fe events	^{60}Fe/Fe AMS, $\times 10^{-16}$	^{60}Fe/Fe corr., $\times 10^{-16}$	Deposition rate, at ^{60}Fe·a^{-1}·cm^{-2}	Terrestrial fluence Φ_{ter}, 10^5 at^{60}Fe·cm^{-2}
Core 848	0.0 – 1.8	25	4	$0.3^{+0.2}_{-0.1}$	$0.2^{+0.3}_{-0.2}$	$0.02^{+0.03}_{-0.02}$	$0.10^{+0.18}_{-0.10}$
Core 848	1.8 – 2.6	27	38	4.3 ± 0.9	7.4 ± 1.2	0.50 ± 0.14	4.0 ± 1.0
Core 848	2.6 – 8.0	15	0	<0.3	<0.9	<0.06	<0.48
Core 851	1.6 – 1.8	3	2	$1.6^{+1.8}_{-1.0}$	$2.4^{+2.9}_{-1.6}$	$0.47^{+0.56}_{-0.32}$	$3.4^{+4.5}_{-2.5}$
Core 851	1.8 – 2.6	22	40	2.7 ± 0.4	4.6 ± 0.8	0.92 ± 0.23	7.5 ± 2.5
Core 851	2.6 – 3.7	19	5	$1.1^{+0.6}_{-0.5}$	$2.2^{+1.4}_{-1.1}$	$0.44^{+0.26}_{-0.22}$	$3.5^{+2.0}_{-1.8}$
Blank		18	1	$0.2^{+0.3}_{-0.1}$			

Rows indicate separation of the sediment cores into three intervals. The last row represents data obtained from processing blank material. The corrected (corr.) ^{60}Fe/Fe concentrations are corrected for radioactive decay and the blank level. Fluence is in units of atoms (at) per square centimeter. All errors are given as 1σ uncertainties.

the FeMn crust now becomes $\Phi_{ter}^{crust} = (2.5 \pm 1.3) \times 10^6$ at/cm^2, which is about a factor of 4 to 5 higher than our result and does not take an uptake efficiency for Fe of the FeMn crust into account. Interestingly, another recently reported fluence value deduced from Indian Ocean sediments (48) ($\Phi_{ter}^{ind} = (35.4 \pm 2.6) \times 10^6$ at/cm^2) is one to two orders of magnitude higher than the value reported in this work. Possible explanations for such differences are (*i*) a nonuniform ^{60}Fe deposition at the respective locations of the geological reservoirs (see, e.g., ref. 49) and (*ii*) a selective chemical Fe uptake from bottom water currents at certain locations leading to fluence values above those related to the depositional flux.

Conclusions

In summary, we have extracted magnetofossils and other iron-bearing secondary minerals from two Pacific Ocean sediment cores, 848 and 851 of the ODP Leg 138. Using AMS on samples derived from these mineral phases, we have detected a time-resolved ^{60}Fe signal, and this signal coincides with independently observed ones in a deep ocean FeMn crust (11, 12). In view of our results here, we would also note that the North Atlantic sediment results of ref. 12 possibly show a weak ^{60}Fe signal in the same time range as ours. More recently, two other studies have found a compatible ^{60}Fe signature in lunar samples (13) and in Indian Ocean marine sediments (48), with high statistical significance. Our results derive from two independent Pacific Ocean sediment cores, each possessing a continuous time record spanning the entire time window of the ^{60}Fe signal and with no detectable changes in sedimentation rate (Fig. 1 and Fig. S8), no detectable changes of the depositional environment, and a relatively constant concentration of magnetofossils (Fig. S1 and ref. 34) across the time span of the ^{60}Fe signal. For these reasons, our cores 848 and 851 data should be faithful recorders of the temporal profile of the SN material during its arrival on Earth. Fig. S7 (see *Supporting Information*) shows the half-life corrected flux of ^{60}Fe into the sediments and, thus, represents the intrinsic temporal structure of the ^{60}Fe signal. Because our Fe extraction protocol specifically targets authigenic Fe oxides including magnetofossils, rather than the total Fe mineral pool (which is ∼3% of dry sediment mass), as would aggressive leaching procedures, we potentially avoided a ^{60}Fe dilution by up to approximately two orders of magnitude, because the majority of the total Fe mass is of detrital origin. This conclusion is supported by the fact that only ∼1% of the total Fe mineral pool is extracted by the CBD procedure (see *Supporting Information*), which, as seen with magnetic minerals, does not leach lithogenic minerals. Such a strong dilution would have placed our ^{60}Fe/Fe ratio below the blank level, and thereby beyond detectability.

We attribute this ^{60}Fe signal to SN provenance, rather than to micrometeorites, for the following reasons: First, MTB are expected to obtain their iron budget from poorly crystalline hydroxides (see *Supporting Information*), and not from silicate and magnetite micrometeorite grains of >20 μm diameter (14); second, our CBD protocol was designed to selectively dissolve only fine-grained magnetite less than 200 nm in size, thereby avoiding dissolution of any large-scale micrometeorites. Thus, the ^{60}Fe we have extracted cannot be from such micrometeorites.

The Local Bubble (50) is a low-density cavity ∼150 parsecs (pc; 1 pc = 3.09×10^{16} m) in diameter, within the interstellar medium of our galactic arm, in which the solar system presently finds itself. It has been carved out by a succession of ∼20 SNs over the course of the last ∼10 Ma, likely having originated from progenitors in the Scorpius–Centaurus OB star association (50, 51), a gravitationally unbound cluster of stars ∼50 pc in radius. Analyses (51, 52) of the relative motion of this star association have shown that, around 2.3 Ma, it was located at a minimum distance of ∼100 pc from the solar system, making it the most plausible host for any SN responsible for our ^{60}Fe signal. The geological time span covered by our ^{60}Fe signal is intriguing, in that there is an established and overlapping marine extinction event of mollusks (53, 54), marine snails (55), and bivalve fauna (56, 57), in addition to a coeval global cooling period (56–58). The question whether this SN could have contributed to this extinction has been previously raised (51), where it is considered that a SN-induced UV-B catastrophe (59), and its concomitant knock-on effects in the marine biosphere via phytoplankton die off, could have been a proximate factor in this extinction. However, consensus now indicates that a canonical CCSN would need to be within 10 pc of our solar system for there to be a significant and lasting depletion of the ozone layer strong enough to give rise to sudden extinction events (60–62), disfavoring a direct and sudden causal connection, such as a UV-B catastrophe, between a Scorpius–Centaurus CCSN and the Plio-Pleistocene marine extinction.

ACKNOWLEDGMENTS. We are grateful to three anonymous reviewers for their constructive comments, which helped improve the original manuscript, and to the operators of the MLL and the Ion Beam Center at Helmholtz-Zentrum Dresden-Rossendorf for their help during beamtimes. The search for ^{60}Fe supernova signatures is supported by the German Research Foundation (DFG), Grant DFG-Bi1492/1-1, and by the DFG Cluster of Excellence "Origin and Structure of the Universe" (www.universe-cluster.de).

1. Limongi M, Chieffi A (2006) The nucleosynthesis of ^{26}Al and ^{60}Fe in solar metallicity stars extending in mass from 11 to 120 M$_\odot$: The hydrostatic and explosive contributions. *Astrophys J* 647(1):483–500.
2. Rugel G, et al. (2009) New measurement of the ^{60}Fe half-life. *Phys Rev Lett* 103(7):072502.
3. Wallner A, et al. (2015) Settling the half-life of ^{60}Fe: Fundamental for a versatile astrophysical chronometer. *Phys Rev Lett* 114(4):041101.
4. Wang W, et al. (2007) SPI observations of the diffuse ^{60}Fe emission in the Galaxy. *Astron Astrophys* 469(3):1005–1012.
5. Knie K, et al. (1999) Indication for supernova produced ^{60}Fe activity on Earth. *Phys Rev Lett* 83(1):18–21.
6. Athanassiadou T, Fields B (2011) Penetration of nearby supernova dust in the inner solar system. *New Astron* 16(4):229–241.
7. Gomez H (2014) Astrophysics: Survival of the largest. *Nature* 511(7509):296–297.
8. Gall C, et al. (2014) Rapid formation of large dust grains in the luminous supernova 2010jl. *Nature* 511(7509):326–329.
9. Plane JM (2012) Cosmic dust in the earth's atmosphere. *Chem Soc Rev* 41(19):6507–6518.

10. Jickells TD, et al. (2005) Global iron connections between desert dust, ocean biogeochemistry, and climate. *Science* 308(5718):67–71.
11. Knie K, et al. (2004) ^{60}Fe anomaly in a deep-sea manganese crust and implications for a nearby supernova source. *Phys Rev Lett* 93(17):171103.
12. Fitoussi C, et al. (2008) Search for supernova-produced ^{60}Fe in a marine sediment. *Phys Rev Lett* 101(12):121101.
13. Fimiani L, et al. (2016) Interstellar ^{60}Fe on the surface of the Moon. *Phys Rev Lett* 116(15):151104.
14. Stuart F, Lee M (2012) Micrometeorites and extraterrestrial He in a ferromanganese crust from the Pacific Ocean. *Chem Geol* 322–323:209–214.
15. Kachelrieβ M, Neronov A, Semikov DV (2015) Signatures of a two million year old supernova in the spectra of cosmic ray protons, antiprotons, and positrons. *Phys Rev Lett* 115(18):181103.
16. Zachara J, Kukkadapu R, Fredrichson J, Groby Y, Smith S (2002) Biomineralization of poorly crystalline Fe(III) oxides by dissimilatory metal reducing bacteria (DMRB). *Geomicrobiol J* 19(2):179–207.
17. Bellini S (2009) On a unique behaviour of freshwater bacteria. *Chin J Oceanol Limnol* 27(1):3–5.
18. Blakemore R (1975) Magnetotactic bacteria. *Science* 190(4212):377–379.
19. Faivre D, Schüler D (2008) Magnetotactic bacteria and magnetosomes. *Chem Rev* 108(11):4875–4898.
20. Bazylinski DA, Frankel RB (2004) Magnetosome formation in prokaryotes. *Nat Rev Microbiol* 2(3):217–230.
21. Petermann H, Bleil U (1993) Detection of live magnetotactic bacteria in South Atlantic deep-sea sediments. *Earth Planet Sci Lett* 117(1-2):223–228.
22. Kopp R, Kirschvink J (2008) The identification and biogeochemical interpretation of fossil magnetotactic bacteria. *Earth Sci Rev* 86(1):42–61.
23. Konhauser K, Kappler A, Roden E (2011) Iron in microbial metabolism. *Elements* 7(2): 89–93.
24. Roden E, Zachara J (1996) Microbial reduction of crystalline iron(III) oxides: influence of oxide surface area and potential for cell growth. *Environ Sci Technol* 30(5): 1618–1628.
25. Zachara J, et al. (1998) Bacterial reduction of crystalline Fe(III) oxides in single phase suspensions and subsurface materials. *Am Mineral* 83(11):1426–1443.
26. Bosch J, Heister K, Hofmann T, Meckenstock RU (2010) Nanosized iron oxide colloids strongly enhance microbial iron reduction. *Appl Environ Microbiol* 76(1):184–189.
27. Yan L, et al. (2012) Magnetotactic bacteria, magnetosomes and their application. *Microbiol Res* 167(9):507–519.
28. Roberts A, Chang L, Heslop D, Florindo F, Larrasoaña J (2012) Searching for single domain magnetite in the 'pseudo-single-domain' sedimentary haystack: Implications of biogenic magnetite preservation for sediment magnetism and relative paleointensity determinations. *J Geophys Res* 117(B8):B08104.
29. Ludwig P, et al. (2013) Characterization of primary and secondary magnetite in marine sediment by combining chemical and magnetic unmixing techniques. *Global Planet Change* 110(Part C):321–339.
30. Egli R (2004) Characterization of individual rock magnetic components by analysis of remanence curves, 1. Unmixing natural sediments. *Stud Geophys Geod* 48(2):391–446.
31. Egli R, Chen A, Winkelhofer M, Kodama K, Horng C (2010) Detection of noninteracting single domain particles using first-order reveral curve diagrams. *Geochem Geophys Geosyst* 11(1):Q01Z11.
32. Sobolev D, Roden EE (2002) Evidence for rapid microscale bacterial redox cycling of iron in circumneutral environments. *Antonie van Leeuwenhoek* 81(1-4):587–597.
33. Taylor K, Macquaker J (2011) Iron minerals in marine sediments record chemical environments. *Elements* 7(2):113–118.
34. Bishop S, Egli R (2011) Discovery prospects for a supernova signature of biogenic origin. *Icarus* 212(2):960–962.
35. Rowan C, Roberts A, Broadbent T (2009) Reductive diagenesis, magnetic dissolution, greigite growth and paleomagnetic smoothing in marine sediments: A new review. *Earth Planet Sci Lett* 277(1):223–235.
36. Roden E (2004) Analysis of long-term bacterial vs chemical Fe(III) oxide reduction kinetics. *Geochim Cosmochim Acta* 68(15):3205–3216.
37. Mehra O, Jackson M (1958) Iron oxide removal from soils and clays by a dithionite-citrate system buffered with sodium bicarbonate. *Clays Clay Miner* 7(1):317–327.
38. Hunt C, Singer M, Kletetschka G, TenPas J, Verosub K (1995) Effect of citrate-bicarbonate-dithionite treatment on fine-grained magnetite and maghemite. *Earth Planet Sci Lett* 130(1):87–94.
39. Vidic N, TenPas J, Verosub K, Singer M (2000) Separation of pedogenic and lithogenic components of magnetic susceptibility in the Chinese loess/paleosol sequence as determined by the CBD procedure and a mixing analysis. *Geophys J Int* 142(2): 551–562.
40. Mayer L, et al. (1992) Shipboard Scientific Party, 1992: Site 848. *Proc Ocean Drill Program Initial Rep* 138:677–734.
41. Billeaud L, Lewis Pratson E, Broglia C, Lyle M, Dadey K (1995) Data report: Geochemical logging results from three lithospheric plates; Cocos, Nazca, and Pacific: Leg 138, sites 844 through 852. *Proc Ocean Drill Program Sci Results* 138:857–884.
42. Shackleton N, Crowhurst S, Hagelberg T, Pisias N, Schneider D (1995) A new late neogene time scale: Application to leg 138 sites. *Proc Ocean Drill Program Sci Results* 138:73–101.
43. Farrell J, et al. (1995) Late Neogene sedimentation patterns in the Eastern Equatorial Pacific Ocean. *Proc Ocean Drill Program Sci Results* 138:717–756.
44. Knie K, et al. (2000) High-sensitivity AMS for heavy nuclides at the Munich Tandem Accelerator. *Nucl Instrum Methods Phys Res B* 172(1-4):717–720.
45. Cousins R, Linnemann J, Tucker J (2008) Evaluation of three methods for calculating statistical significance when incorporating a systematic uncertainty into a test of the background-only hypothesis for a Poisson process. *Nucl Instrum Methods Phys Res A* 595(2):480–501.
46. Chmeleff J, Blanckenburg FV, Kossert K, Jakob D (2010) Determination of the ^{10}Be half-life by multicollector ICP-MS and liquid scintillation counting. *Nucl Instrum Methods Phys Res B* 268(2):192–199.
47. Korschinek G, et al. (2010) A new value for the half-life of ^{10}Be by heavy-ion elastic recoil detection and liquid scintillation counting. *Nucl Instrum Methods Phys Res B* 268(2):187–191.
48. Wallner A, et al. (2016) Recent near-Earth supernovae probed by global deposition of interstellar radioactive ^{60}Fe. *Nature* 532(7597):69–72.
49. Fry B, Fields B, Ellis J (2016) Radioactive iron rain: Transporting ^{60}Fe in supernova dust to the ocean floor. arXiv:1604.00958.
50. Maíz Appelíniz J (2001) The origin of the local bubble. *Astrophys J* 560:L83–L86.
51. Benítez N, Maíz-Apellániz J, Canelles M (2002) Evidence for nearby supernova explosions. *Phys Rev Lett* 88(8):081101.
52. Breitschwerdt D, et al. (2016) The locations of recent supernovae near the Sun from modelling ^{60}Fe transport. *Nature* 532(7597):73–76.
53. Allmon WD, Rosenberg G, Portell RW, Schindler KS (1993) Diversity of Atlantic coastal plain mollusks since the Pliocene. *Science* 260(5114):1626–1629.
54. Petuch EJ (1995) Molluscan diversity in the late neogene of Florida: Evidence for a two-staged mass extinction. *Science* 270(5234):275–277.
55. Dietl GP, Herbert GS, Vermeij GJ (2004) Reduced competition and altered feeding behavior among marine snails after a mass extinction. *Science* 306(5705):2229–2231.
56. Raffi S, Stanley SM, Marasti R (1985) Biogeographic patterns and Plio-Pleistocene extinction of Bivalvia in the Mediterranean and southern North Sea. *Paleobiology* 11(4):368–388.
57. Stanley SM (1986) Anatomy of a regional mass extinction: Plio-Pleistocene decimation of the western Atlantic bivalve fauna. *Palaios* 1(1):17–36.
58. Berkman PA, Prentice ML (1996) Pliocene extinction of Antarctic pectinid mollusks. *Science* 271(5255):1606–1607.
59. Cockell CS (1999) Crises and extinction in the fossil record—A role for ultraviolet radiation? *Paleobiology* 25(2):212–225.
60. Gehrels N, et al. (2003) Ozone depletion from nearby supernovae. *Astrophys J* 585(2):1169–1176.
61. Beech M (2011) The past, present and future supernova threat to Earth's biosphere. *Astrophys Space Sci* 336(2):287–302.
62. Melott A, Thomas BC (2016) Brief review and census of intermittent intense sources. arXiv:1605.04926v1.
63. Raiswell R (2011) Iron transport from the continents to the open ocean: The aging-rejuvination cycle. *Elements* 7(2):101–106.
64. Watkins S, Maher B (2003) Magnetic characterization of present-day deep-sea sediments and sources in the North Atlantic. *Earth Planet Sci Lett* 214(3-4):379–394.
65. Franke C, Dobeneck TV, Drury M, Meeldijk J (2007) Magnetic petrology of equatorial Atlantic sediments: Electron microscopy results and their implications for environmental magnetic interpretation. *Paleoceanography* 22(4):PA4207.
66. Yamazaki T (2009) Environmental magnetism of Pleistocene sediments in the North Pacific and Ontong-Java Plateau: Temporal variations of detrital and biogenic components. *Geochem Geophys Geosyst* 10(7):Q07Z04.
67. Canfield DE (1989) Reactive iron in marine sediments. *Geochim Cosmochim Acta* 53(3):619–632.
68. Fortin D, Langley S (2005) Formation and occurrence of biogenic iron-rich minerals. *Earth Sci Rev* 72(1-2):1–19.
69. Butler R, Banerjee S (1975) Theoretical single-domain grain-size range in magnetite and titatomagnetite. *J Geophys Res* 80(29):4049–4058.
70. Dunlop D, Özdemir Ö (1997) *Rock Magnetism* (Cambridge Univ Press, Cambridge, UK).
71. Lovley D, Stolz J, Nord GL, Jr, Phillips EJP (1987) Anaerobic production of magnetite by a dissimilatory iron-reducing microorganism. *Nature* 330(6145):252–254.
72. Maher B (1988) Magnetic properties of some synthetic sub-micron magnetites. *Geophys J* 94(1):83–96.
73. Devourad B, et al. (1998) Magnetite from magnetotactic bacteria: Size distribution and twinning. *Am Mineral* 83:1387–1398.
74. Fairve D, et al. (2004) Mineralogical and isotopic properties of inorganic nanocrystalline magnetites. *Geochim Cosmochim Acta* 68(21):4395–4403.
75. Egli R, Lowrie W (2002) Anhysteretic remanent magnetization of fine magnetic particles. *J Geophys Res* 107(B10):2209.
76. Snowball I, Zillén L, Sandgren P (2002) Bacterial magnetite in Swedish varved lake-sediments: A potential bio-marker of environmental change. *Quat Int* 88(1):13–19.
77. Wack M, Gilder S (2012) The SushiBar: An automated system for paleomagnetic investigations. *Geochem Geophys Geosyst* 13(3):Q12Z38.
78. Moskowitz B, Frankel R, Bazylinski D (1993) Rock magnetic criteria for the detection of biogenic magnetite. *Earth Planet Sci Lett* 120(3-4):283–300.
79. Dobeneck T, Petersen N, Vali H (1987) Bakterielle Magnetofossilien. *Geowiss Unserer Z* 1:25–27. German.
80. Hounslow M, Maher B (1996) Quantitative extraction and analysis of carriers of magnetization in sediments. *Geophys J Int* 124(1):57–74.
81. Galindo-González C, et al. (2009) Magnetic and microscopic characterization of magnetite nanoparticles adhered to clay surfaces. *Am Mineral* 94(8-9):1120–1129.
82. Baldaug J, Iwai M (1995) Neogene diatom biostratigraphy for the eastern equatorial Pacific Ocean, Leg 138. *Proc Ocean Drill Program Sci Results* 138:105–128.
83. Gurvich E, Levitan M, Kuzmina T (1995) Chemical composition of Leg 138 sediments and history of hydrothermal activity. *Proc Ocean Drill Program Sci Results* 138:769–778.
84. Mann S, Sparks N, Blakermore R (1987) Structure, morphology, and crystal growth of anisotropic crystals in magnetotactic bacteria. *Proc R Soc Lond B Biol Sci* 231:477–487.
85. Arató B, et al. (2005) Crystal-size and shape distributions of magnetite from uncultured magnetotactic bacteria as a potential biomarker. *Am Mineral* 90(8-9): 1233–1241.

86. Chen A, Egli R, Moskowitz B (2007) First-order reversal curve (FORC) diagrams of natural and cultured biogenic magnetic particles. *J Geophys Res* 112(B8):B08S90.
87. Vali H, Förster O, Amarantidis G, Petersen N (1987) Magnetotactic bacteria and their magnetofossils in sediments. *Earth Planet Sci Lett* 86(2-4):389–400.
88. Hejda P, Zelinka T (1990) Modelling of hysteresis processes in magnetic rock samples using the Preisach diagram. *Phys Earth Planet Inter* 63(1-2):32–40.
89. Pike C, Fernandez A (1999) An investigation of magnetic reversal in submicron-scale Co dots using first order reversal curve diagrams. *J Appl Phys* 85(9):6668–6676.
90. Mayergoyz ID (1986) Mathematical models of hysteresis. *Phys Rev Lett* 56(15):1518–1521.
91. Preisach F (1935) Über die magnetische Nachwirkung. *Z Phys* 94(5):277–302. German.
92. Néel L (1958) Sur les effets d'un couplage entre grains ferromagnétiques doués d'hystérésis. *Acad Sci Seance* 24(4):2313–2319. French.
93. Roberts A, Pike C, Verosub K (2000) First-order reversal curve diagrams: A new tool for characterizing the magnetic properties of natural samples. *J Geophys Res* 105(B12):28461–28475.
94. Roberts A, et al. (2006) Characterization of hematite (alpha-$Fe^{2}O^{3}$), geothite (alpha-FeOOH), greigite ($Fe^{3}S^{4}$), and pyrrhotite ($Fe^{7}S^{8}$) using first-order reversal curve diagrams. *J Geophys Res* 111(B12):B12S35.
95. Muxworthy A, Williams W (2005) Magnetostatic interaction fields in first-order-reversal-curve diagrams. *J Appl Phys* 97(6):063905.
96. Newell A (2005) A high-precision model of first-order reversal curve (FORC) functions for single-domain ferromagnets with uniaxial anisotropy. *Geochem Geophys Geosyst* 6(5):Q05010.
97. Egli R (2013) VARIFORC: An optimized protocol for the calculating non-regular first-order reversal curves (FORC) diagrams. *Global Planet Change* 110(Part C):302–320.
98. Heslop D, et al. (2013) Quantifying magnetite magnetofossil contributions to sedimentary magnetizations. *Earth Planet Sci Lett* 382:58–65.
99. Heslop D, Roberts A, Chang L (2014) Characterizing magnetofossils from first-order reversal curve (FORC) central ridge signatures. *Geochem Geophys Geosyst* 15(6):2170–2179.
100. Kobayashi A, et al. (2006) Experimental observation of magnetosome chain collapse in magnetotactic bacteria: Sedimentological, paleomagnetic, and evolutionary implications. *Earth Planet Sci Lett* 245:538–550.
101. Straub S, Schmincke H (1998) Evaluating the tephra input into Pacific Ocean sediments: Distribution in space and time. *Geol Rundsch* 87(3):461–476.
102. Fu Y, Von Dobeneck T, Franke C, Heslop D, Kasten S (2008) Rock magnetic identification and geochemical process models of greigite formation in Quaternary marine sediments from the Gulf of Mexico, (IODP Hole U1319A). *Earth Planet Sci Lett* 275:233–245.
103. Pisias N, Mayer L, Mix A (1995) Paleoceanography of the eastern equatorial Pacific during the Neogene: synthesis of Leg 138 drilling results. *Proc Ocean Drill Program Sci Results* 138:5–21.
104. Merchel S, Herpers U (1999) An update on radiochemical separation techniques for the determination of long-lived radionuclides via accelerator mass spectrometry. *Radiochim Acta* 84(4):215–219.
105. Schubert M (2007) Radioaktive implantate für medizinische anwendungen. PhD thesis (Ludwig-Maximilians-Universität, Munich).
106. Middleton R (1983) A versatile high intensity negative ion source. *Nucl Instrum Methods Phys Res* 214(2-3):139–150.
107. Urban A (1986) Beschleunigermassenspektrometrie mit ^{41}Ca. Diploma thesis (Tech Univ München, Munich).
108. Feldmann G, Cousins R (1998) A unified approach to the classical statistical analysis of small signals. *Phys Rev D Part Fields* 57(7):3873–3889.
109. Bourlès D, Raisbeck G, Yiou F (1989) ^{10}Be and ^{9}Be in marine sediments and their potential for dating. *Geochim Cosmochim Acta* 53(2):443–452.
110. Feige J, et al. (2013) AMS measurements of cosmogenic and supernova-ejected radionuclides in deep-sea sediment cores. arXiv.1311.3481.
111. Akhmadaliev S, Heller R, Hanf D, Rugel G, Merchel S (2013) The new 6 MV AMS-facility DREAMS at Dresden. *Nucl Instrum Methods Phys Res B* 294:5–10.